Macro and nanoscale wear behaviour of Al-Al_2O_3 nanocomposites fabricated by selective laser melting

Quanquan Han[a], Yanquan Geng[a,b], Rossitza Setchi[a]*, Franck Lacan[a], Dongdong Gu[c], Sam L. Evans[a]

[a] Cardiff School of Engineering, Cardiff University, Cardiff CF24 3AA, UK

[b] Centre for Precision Engineering, Harbin Institute of Technology, Harbin, PR China

[c] College of Materials Science and Technology, Nanjing University of Aeronautics and Astronautics, Nanjing, PR China

Corresponding author: Rossitza Setchi, Setchi@cardiff.ac.uk, +44(0)2920875720

Abstract

Aluminium-based composites are increasingly applied within the aerospace and automotive industries. Tribological phenomena such as friction and wear, however, negatively affect the reliability of devices that include moving parts; the mechanisms of friction and wear are particularly unclear at the nanoscale. In the present work, pin-on-disc wear testing and atomic force microscopy nanoscratching were performed to investigate the macro and nanoscale wear behaviour of an Al-Al_2O_3 nanocomposite fabricated using selective laser melting. The experimental results indicate that the Al_2O_3 reinforcement contributed to the macroscale wear-behaviour enhancement for composites with smaller wear rates compared to pure Al. Irregular pore surfaces were found to result in dramatic fluctuations in the frictional coefficient at the pore position within the nanoscratching. Both the size effect and the working-principle difference contributed to the difference in frictional coefficients at both the macroscale and the nanoscale.

Keywords: A. Metal-matrix composites (MMCs), B. Wear, B. Porosity, B. Microstructures

1. Introduction

Aluminium-based metal matrix composites (AMCs) are widely used in the aerospace, defence and automotive industries because of these materials' lightness, high specific strength, excellent wear resistance and controllable expansion coefficient [1-3]. Brake rotors, pistons and connecting rods are among the better-known applications of AMCs in the automotive industry [4]. A wide range of

reinforcement particulates, including Al_2O_3, SiC, B_4C, TiC and TiO_2, are generally used [5]. Compared to other reinforcements, however, nanoscale Al_2O_3 particulates are capable of improving both their wear behaviour and their high-temperature properties without introducing any undesirable phases; for this reason, nanoscale Al_2O_3 particulates are widely used with AMCs [6].

Tribological phenomena such as friction and wear are significant determiners of the life and performance of assemblies with moving parts. The mechanisms of friction and wear are particularly unclear at the nanoscale, which limits the development of microsystems technologies [7]. Atomic force microscopy (AFM) is widely used in various nanotechnology and nanomanufacturing applications because of its low cost and its ability to achieve atomic-level manipulation using a relatively simple system. Because AFM is capable of applying extremely small forces and visualising surface topography with a resolution below 0.1 nm [8,9], the method can thus be used to investigate nanoscale friction and wear behaviour. Another advantage of AFM is that the technique can simulate a single-asperity contact situation against a counter surface, which provides a way to investigate the friction mechanisms involved in ultra-precise components. The basic operating principle of AFM involves scanning a specimen surface under a controlled load using a sharp tip, normally made of silicon, silicon nitride or a diamond coating; the sensors that are employed can then detect atomic-scale interaction forces with a nano-Newton resolution [7,10,11].

Fabricating the customised and functional components that are used in the aerospace and automotive industries, however, is always a challenge when using traditional manufacturing technologies. Based on the layer-by-layer manufacturing principle, additive manufacturing (AM) technology provides an integrated way to manufacture three-dimensional (3D) complex-shaped components from computer-aided design files; AM is one of the most rapidly developing advanced manufacturing technologies in the world [12-14]. Amongst current AM techniques, selective laser melting (SLM) is widely used to manufacture 3D complex-shaped metallic parts [15]. The SLM of Al-Al_2O_3 nanocomposites thus has significant potential for the fabrication of advanced engineering components. Furthermore, the development of SLM technology has led to composite materials finding more applications in aerospace and automotive industries. Recently, interest has emerged with regard to using SLM

to manufacture micro-electro-mechanical systems (MEMS) [16] such as MEMS gyroscopes that are widely used in modern cars and planes. The wear behaviour may be a significant determiner of their life and performance; due to the length scale limitation, the macro wear test (e.g. pin-on-disc testing) is inapplicable to study the wear behaviour however, the micro wear test (e.g. AFM nanoscratching) is thereby employed to study the nanoscale wear behaviour in order to predict and improve the life and performance of the MEMS gyroscopes.

Porosity is the primary defect to occur during the SLM process; pores may be categorised as either metallurgical pores or keyhole pores [17,18]. Ideally, parts should be produced without porosity, since this defect can significantly influence friction and wear behaviour, particularly with nanoscale tribological performance. Several recent studies have reported the macroscale wear performance of parts that were fabricated by SLM and other conventional processes. For instance, Kang et al. [19] employed dry sliding to investigate the wear behaviour of hypereutectic Al-Si alloys fabricated by SLM and found that nanosize Si particles grew to become larger particles due to extended solidification times when the laser power was greater than 210 W, which in turn resulted in poor wear resistance of the fabricated samples. Jue et al. studied the microstructure and mechanical properties of SLM-fabricated Al-based composites and found that the microstructural features and hardness of the composites were the dominating factors to determine wear performance during pin-on-disc testing [20]. Sun et al. investigated the sliding wear characteristics of SLM 316L stainless steel and found that the wear rate of SLM steel was dependent on the porosity and by obtaining full density it was possible to achieve wear resistance similar to that of standard bulk 316L steel [21]. Baradeswaran and Perumal investigated the wear characteristic of Al 7075/graphite composites that were fabricated using conventional liquid casting technique; their study found that the wear rate decreased with addition of graphite content and reached the minimum at 5 wt.% graphite [22]. Lacob et al. studied the wear rate of the Al/Al_2O_3/Gr hybrid composites produced via powder metallurgy and found that a low wear rate exhibited by the composites because of the presence of Al_2O_3 and Gr which functioned as load bearing and solid lubricant, respectively [23].

The effects of surface roughness and rugged topography on friction behaviour are well known, but the influence of the particular shape of keyhole pores that are

formed during SLM on the nanoscale friction and wear behaviour has not previously been investigated. Accordingly, the aim of the current work is to employ pin-on-disc tribometry and AFM nanoscratching to investigate both the macroscale and nanoscale wear behaviour of SLM-fabricated composite specimens. The study examines the influences of Al_2O_3 reinforcement on macroscale-wear performance using pin-on-disc wear sliding; it also investigates the influences of keyhole pores on frictional-coefficient distribution under different applied normal loads using AFM nanoscratching. The contact of the AFM tip with the composite samples is similar to the contact of asperities during two surfaces sliding, and so investigating this adds to the understanding of micro- and macro scale friction behaviour. The study of micro behaviour also contributes to understanding the influence of different phases (Al and Al_2O_3 in present work) on microscale behaviour (e.g. friction and wear) within composites.

2. Materials and methods

2.1. Materials and sample preparation

The materials used in this study included gas-atomised Al (-325 mesh, 99.5%) acquired from the Alfa Aesar Corporation (Ward Hill, Mass., USA) and Al_2O_3 powder (50 nm) obtained from Sigma-Aldrich Ltd. (Dorset, UK). A laboratory planetary mill with four working stations (PULVERISETTE 5 classic line, Fritsch GmbH, Idar-Oberstein, Germany) was employed to ball-mill the composite powder, which was comprised of 96 vol.% Al and 4 vol.% Al_2O_3 powder. The balling process was conducted under an argon atmosphere for up to 20 hours by employing a 10-minute milling and 15-minute pause combination. The ball-milled composite powder after 20 hours of milling was found to exhibit proper flowability, while the Al_2O_3 reinforcement was found to have been distributed uniformly amongst the Al matrix. Fig. 1a shows the morphology of the composite power after ball-milling for 20 hours. More details on the process of the ball-milled composite powder may be found in the authors' previous publications [24,25].

A Renishaw AM250 (Renishaw Plc, New Mill, UK) SLM system that employs a modulated ytterbium-fibre laser with a wavelength of 1,071 nm was used to prepare 8 x 8 x 8 mm cubic samples. The samples were built within an argon atmosphere to minimise oxidation during the processing. A striped fill-hatch-type scanning strategy

was employed for the study; the rotational angle between each adjacent layer was set to 67° to eliminate the chance of scan lines repeating themselves directly on top of one another (which would create poor material properties). The cubic samples were fabricated under the optimum condition of 200 W laser power and an exposure time of 250 µs, which is equivalent to a 300 mm/s scanning speed (Fig. 1b). Fig. 1c shows the top surface of a polished sample in which a few keyhole pores and microcracks have formed. The porosity on the composite specimen surface (Fig. 1c) was evaluated using ImageJ software, and was found to be 0.168%. The average circularity of the keyhole pores was 0.812 and the measured pore size varied from 10 to 38 µm with an average value of 22.4 µm. Furthermore, the as-fabricated cubic samples were both horizontally and vertically sectioned to investigate the spatial distribution of Al_2O_3 particulates; the Al_2O_3 particulates were found to distribute fairly uniformly amongst the Al matrix. Fig. 1d shows the distribution of Al_2O_3 particulates in the vertically sectioned cubic sample. The distribution density of Al_2O_3 was also evaluated using ImageJ software, and was found to be 13.9%; the circularity of the measured Al_2O_3 particulates was 0.81 with an average size of 350 nm; a few clusters were still formed though.

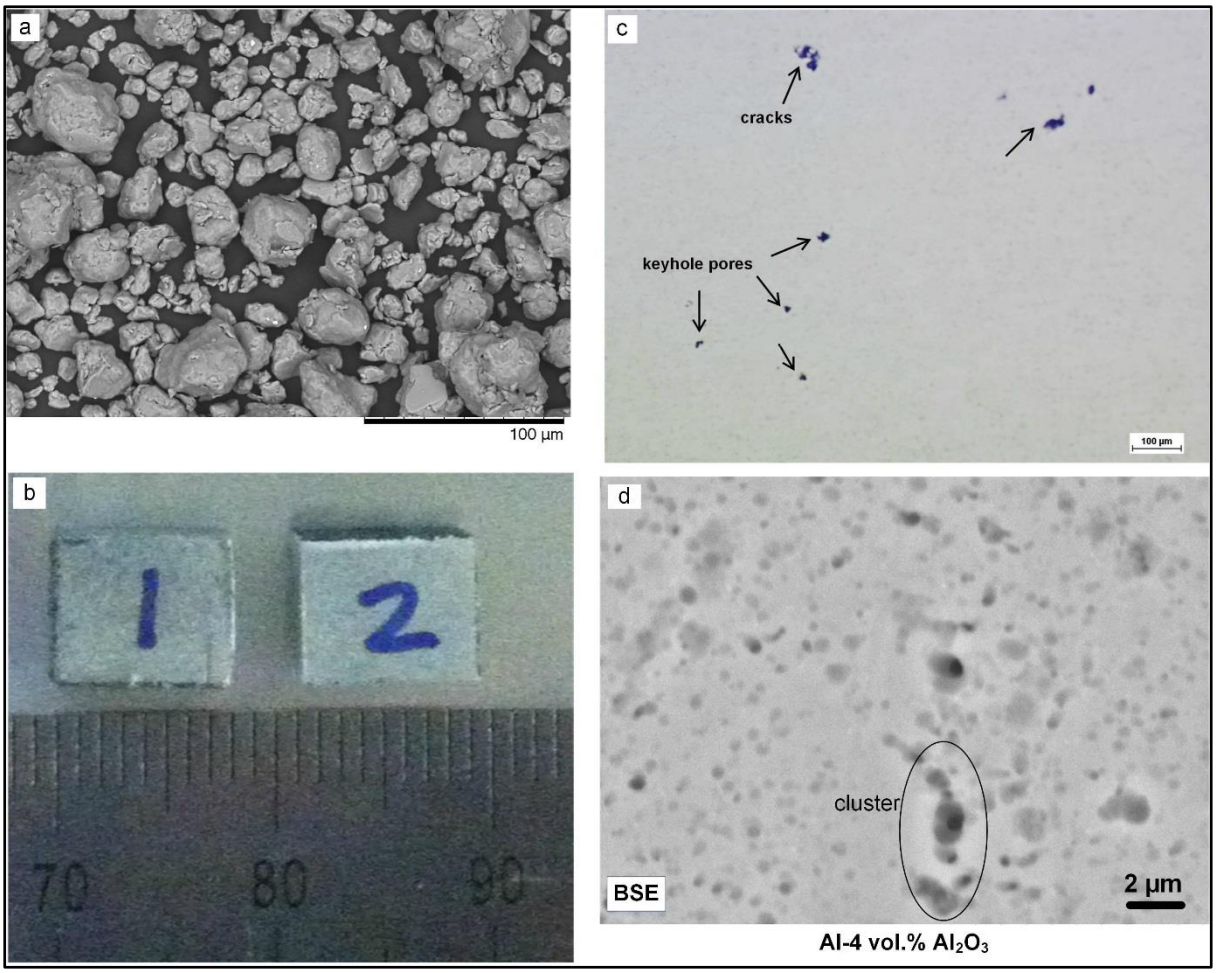

Fig. 1. Images showing (a) ball-milled composite powder; (b) as-fabricated samples; (c) porosity of the sample on the top surface; (d) distribution of Al_2O_3 particulates in vertically sectioned cubic sample.

2.2. Analytical techniques

An in-house developed pin-on-disc tribometer was used to conduct the macroscale wear test at room temperature. The normal load to be applied was set to be 1N for the as-fabricated composite and pure Al samples. The rotation diameter, sliding speed and sliding time were 7 mm, 25 rpm and 30 min, respectively. The frictional coefficient (μ) was recorded during the wear tests. The wear rate (ω) may be expressed as:

$$\omega = \frac{V_\Delta}{N \cdot L} \qquad (1)$$

where V_Δ denotes the volume loss of the specimen, and N and L represent the applied normal load and sliding distance, respectively. V_Δ may be determined by:

$$V_\Delta = \frac{W_\Delta}{\rho} \qquad (2)$$

where W_{Δ} denotes the weight loss of a specimen after the wear test, while ρ is the density of the specimen.

A commercial AFM instrument (Park Systems XE-100, Suwon, South Korea) equipped with a pyramidal diamond tip (DNISP, Veeco Inc., USA; tip radius < 40 nm) was used to scratch the polished composite sample at room. The ambient was temperature controlled, which was 21±0.5 ºC, and the humidity was measured using the rotronic HYGROLOG hygrometer (Crawley, West Sussex, UK), which was 43.2±1.3%. The average spring constant of the cantilever was 221 N/m. The scratching speed was fixed at 2 µm/s, using different normal loads ranging from 10–40 µN in order to investigate the influence of the keyhole pores on the wear behaviour at the nanoscale level. The frictional force (f) under specific normal load during the AFM nanoscratching may be determined by:

$$f = \alpha \cdot M \tag{3}$$

where M denotes the voltage-output difference between the scratching and non-scratching stages; this difference was recorded by the position-sensitive detector (PSD) in the horizontal plane. α represents the conversion factor between the lateral voltage output and the frictional force. More details on the process of determining the value of α may be found in the literature [26,27]. The frictional coefficient was thus obtained by dividing the friction force (f) by the applied normal force (N). The wear rate (ω) within AFM nanoscratching may be attained by dividing the grooved cross-sectional area by the applied normal load. Vickers microhardness tests were performed using Innovatest (Maastricht, Netherlands) with a 100 g load and 10 s dwell time.

3. Results

3.1. Macro-wear behaviour and microstructure

Fig. 2 shows the friction and wear performance of the composite and pure Al samples following the pin-on-disc tests; Fig. 2a shows the frictional-coefficient variation of the composite specimen fabricated at 300 mm/s. The frictional coefficient showed very large fluctuations at the beginning of the sliding stage (because of the vibrations) but tended to be relatively stable afterwards. The average frictional coefficient of the composite specimen was determined to be 0.83 after 30 minutes of sliding. The frictional performance of pure Al exhibited a similar vibrational trend at

the beginning of the sliding stage, although a smaller average frictional coefficient of 0.74 was determined (Fig. 2b).

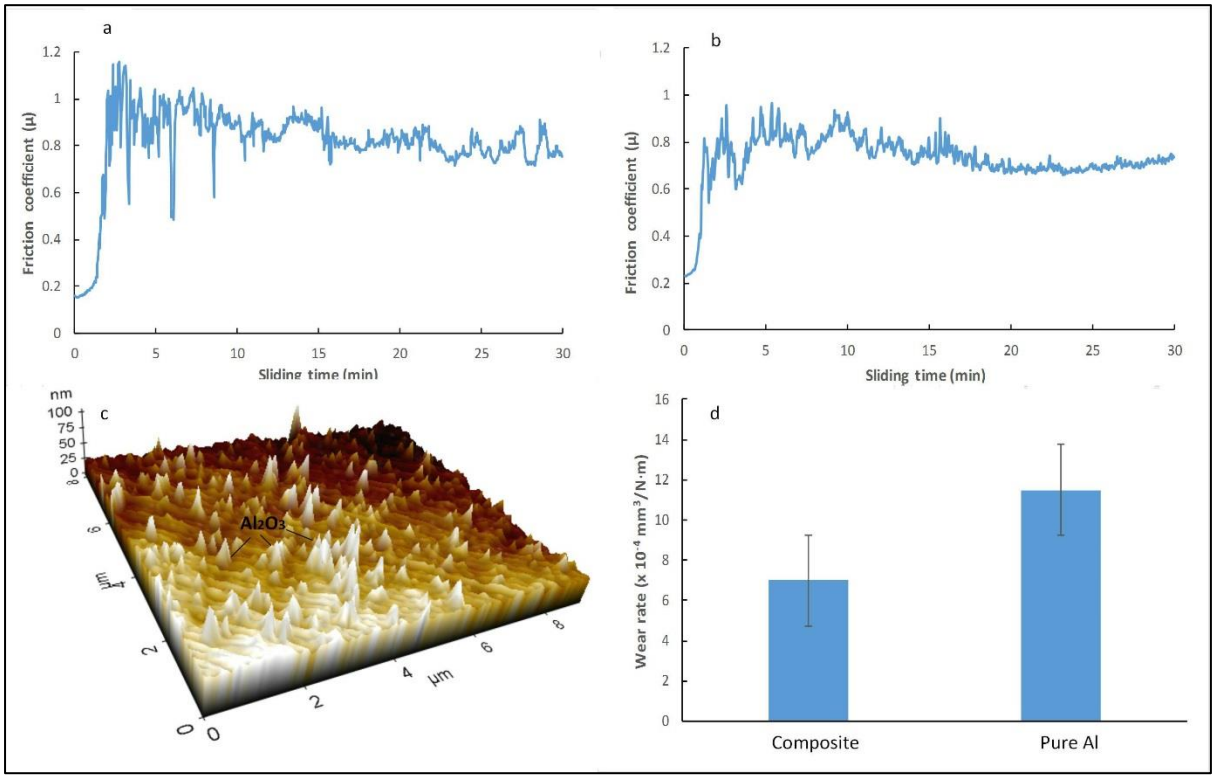

Fig. 2. Friction and wear behaviour: frictional-coefficient variation of (a) composite and (b) pure Al; (c) atomic force microscopy (AFM) 3D topography; (d) wear rate.

In comparison with pure Al, the composite specimen offered a slight improvement in average frictional coefficient, which could be explained by the uniform distribution of the Al_2O_3 reinforcement amongst the Al matrix. Because of the significant hardness difference between the Al_2O_3 and Al phases, part of the Al_2O_3 particulates were exposed outside the Al matrix after the polishing process, which in turn resulted in a rougher surface topography than was the case with the pure Al specimen. This situation was confirmed by the 3D AFM topography image (Fig. 2c). Fig. 2d shows the wear rate of the composite and pure Al specimens after the wear tests (7 and 11.5 x 10^{-4} mm^3/Nm, respectively). Compared to the pure Al specimen, the composite exhibited better wear behaviour with a lower wear rate, which could be attributable to the addition of Al_2O_3 reinforcement.

Scanning electron microscopy (SEM) images of both composites and pure Al specimens following the wear tests are shown in Fig. 3 to help visualise the wear mechanism of SLM-produced composites during these tests. Fig. 3a(1–3) shows the

wear trace of the composite specimen with different magnifications. It is clear that several microchips were produced and narrow grooves were left on the specimen surface (Fig. 3a–3), which implies that the dominating wear mechanism was abrasive wear. It should be noted that the delamination occurred on the composite surface; with continued sliding, the upper layer delaminated from the specimen surface and subsequently formed microchips and wear particles.

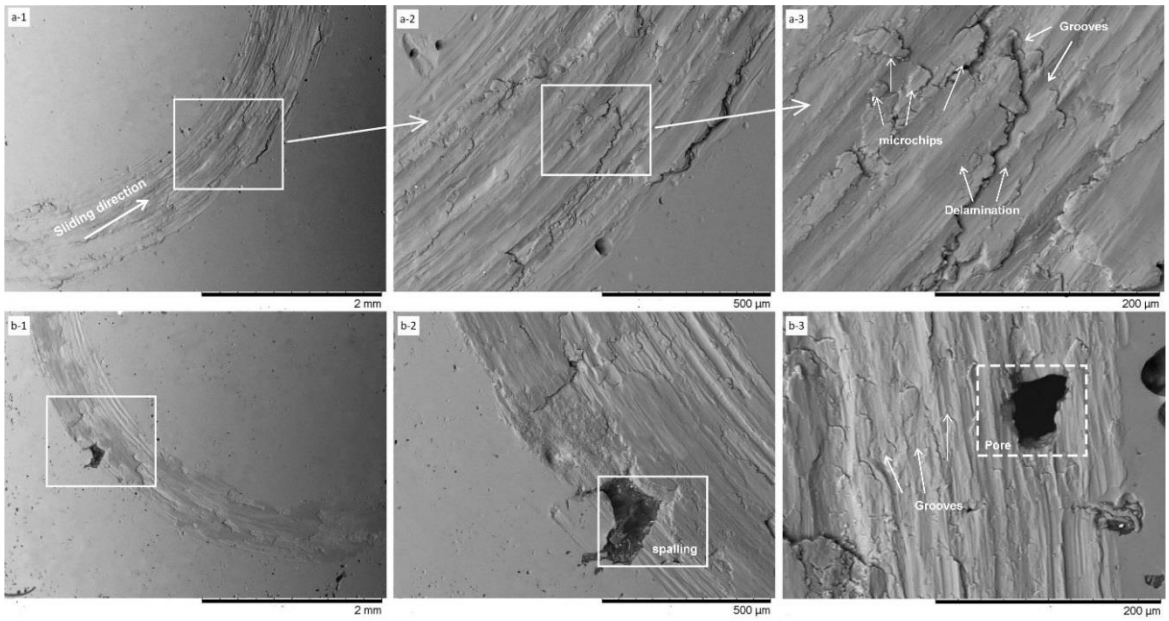

Fig. 3. Scanning electron microscopy (SEM) images showing the worn regions of the composite and pure Al samples.

Compared to the composite specimen, the pure Al specimen tended to offer poorer wear behaviour, and flake spalling was observed on the worn surface (Fig. 3b-2). A larger number of parallel and narrow grooves were formed on the worn specimen surface due to the generation of microchips and wear particles (Fig. 3b-3). Since the Al specimen exhibited higher porosity than the composite specimen, a relatively large pore was also observed on the worn surface of the pure Al specimen.

In addition to the Al_2O_3 reinforcement, the improvement in wear resistance of the composite specimen is also induced by the fine microstructure that was formed during the SLM. Fig. 4 shows the microstructure of the as-fabricated composite sample fabricated at 300 mm/s. Fig. 4a (1–3) shows the microstructure of the as-fabricated horizontally (perpendicular to building direction) sectioned sample with three different magnifications. The molten pool tracks after solidification were clear and intact without obvious porosity present, thus implying that alumina particulates

showed good wetting ability and that dense parts could be produced under the process parameters that were employed. The as-fabricated sample showed a granular microstructure; the microstructure was considered to be that of aluminium caused by the rapid solidification due to the laser irradiation, as reported by Kimura et al. [28]. Furthermore, the microstructure at the molten pool region showed different development; in that case, a relatively fine microstructure was observed within the molten pool as compared to the coarse microstructure found at the boundary regions of the molten pool (Fig. 4a-2, 3).

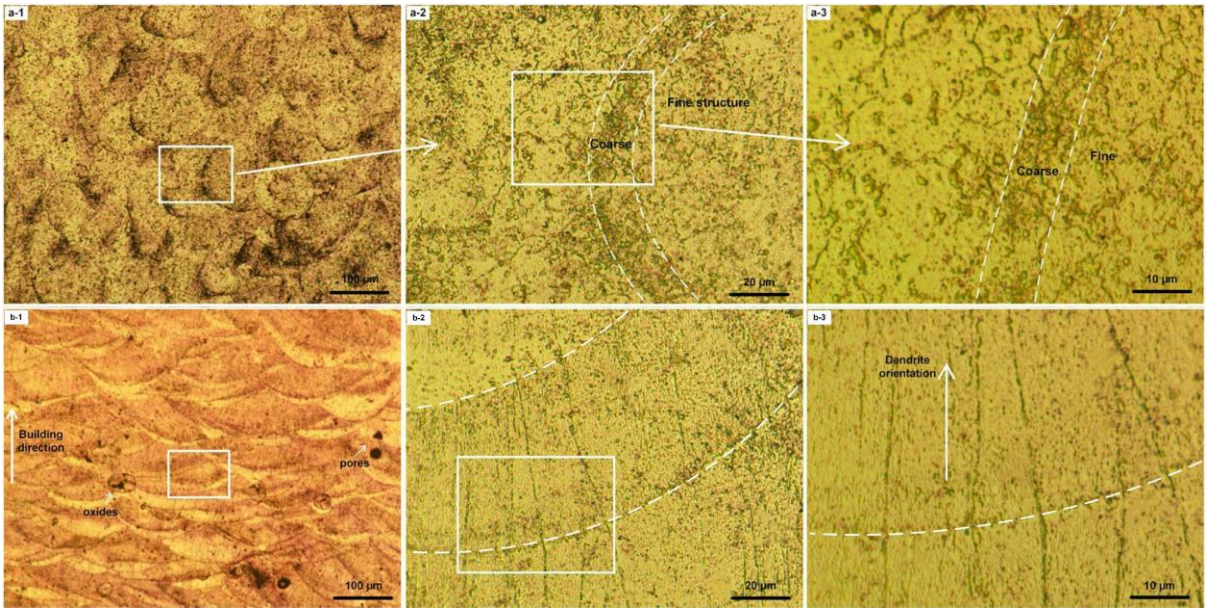

Fig. 4. Optical microscopy (OM) images showing the microstructure of composite samples fabricated at 300 mm/s: (a1-a3) as fabricated horizontal section and (b1-b3) vertical section.

Fig. 4b (1–3) shows the microstructure of an as-fabricated vertically (along the building direction) sectioned composite sample. The formation of semi-circular molten pools was attributable to the Gaussian-distributed heat flux. Molten pools were present at a certain angle, which is thought to have been induced by the rotation angle (67°C) between each adjacent layer. A good metallurgical bonding between two adjacent layers was thus formed under this condition, though some open pores and oxides still remained (Fig. 4b–1). It should be noted that columnar grains were formed and grew along the building direction – or rather they grew along the positive temperature gradient (Fig. 4b 2–3). Generally, during the SLM process, the powder layer is irradiated and the induced heat energy is transferred from the surface of a deposited powder layer to the solidified layers underneath; columnar grains form during the solidification process due to the temperature gradient within

the molten pool. In the present study, the grains that formed in the solidified layers underneath also grew along the temperature gradient and further formed columnar grains because of the heat conduction and remelting process; dendrite microstructures were thus formed (Fig. 4b 2–3).

3.2. nanoscale wear behaviour

Fig. 5a shows a schematic of AFM nanoscratching and the pyramidal diamond tip that was used in this study, with a nominal radius of less than 40 nm, as indicated in the SEM image. Fig. 5b shows a 3D AFM image of the sample that was scratched under the normal load of 30 μN. As the figure shows, a clear groove through a keyhole pore was generated, along with produced pile-up. The lateral voltage output difference and Z signal were then captured (Fig. 5c). The lateral signal was used to determine the friction force during the scratching by using Eq. (3); the conversion factor α was calculated using a standard calibration grating, which was 23.75 μN/V. The *Z* signal output indicates the surface roughness of the scratched path; a hole in the sample surface is generally indicated by a convex shape; a surface hill, in contrast, would be indicated by a concave shape in the captured Z signal graph.

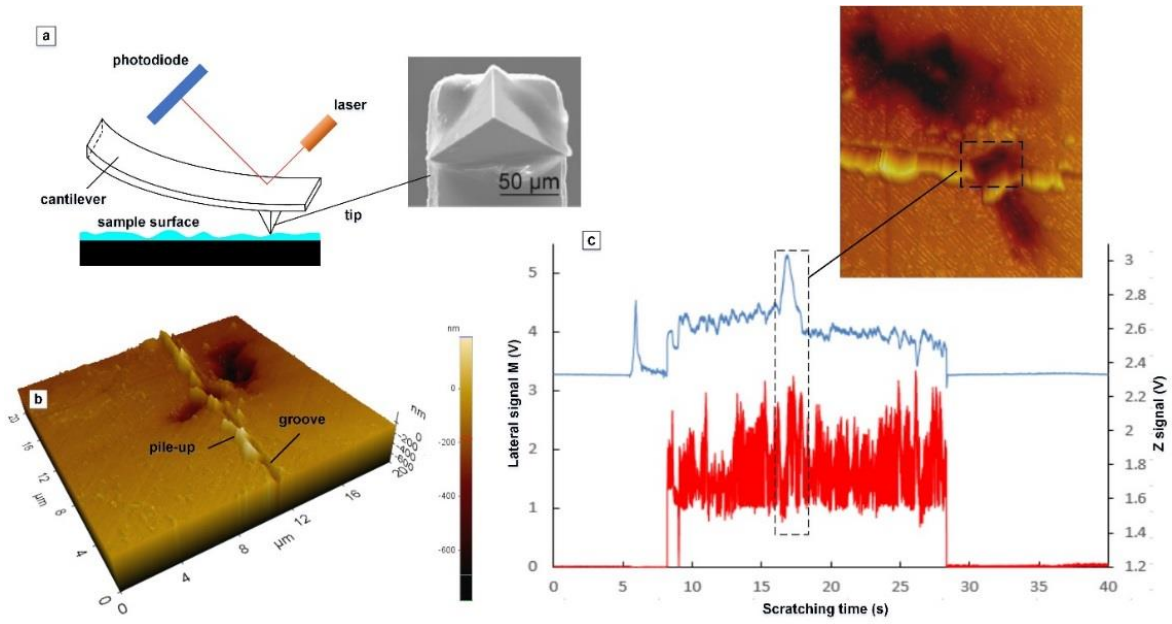

Fig. 5. Scratched sample surface with a pore and detected signals: (a) schematic of the scratching and SEM image of the diamond tip; (b) 3D image of the scratched sample surface; (c) detected lateral voltage output (red line) and *z* signal (blue line) during the scratching.

A clear convex profile was captured in the *Z* signal graph, which indicates that the marked keyhole was scratched and recorded. It should be noted that the lateral signal fluctuated after the beginning of the scratching and continued until the end; this may be explained by the uniform distribution of Al_2O_3 particulates, which were exposed outside the Al matrix after the polishing and thus resulted in a rough sample surface. Another phenomenon that should be mentioned is that the lateral signal experienced relatively dramatic fluctuations at the pore position, which suggests that the pore surface could have an important effect on the friction-force distribution during the AFM scratching.

It should be reminded that keyholes are actually defects that occur during the SLM process and that, ideally, parts should be produced without them, as they could influence the friction and wear behaviour. To further understand the influence of the keyhole pore on friction force during the scratching, Fig. 6a shows a magnification of the lateral signal at the pore position. The figure shows details of the lateral and Z signal's fluctuation within 2 s of scratching; the fluctuation of the lateral-voltage output from roughly 2.8 V to 0.8 V implies an irregularity in the scratched pore surface. Fig. 6b shows the magnification of the pore surface with several marked specific positions (from A to F) in order to clarify the effect of the pore surface on the lateral signal output; the corresponding positions are from A' to F' in the lateral signal graph. Specifically, the scratching starts from position A to position F under a normal load (30 μN) and scratching speed (2 μm/s). Position A is the front edge of this keyhole pore, with a lateral voltage output of roughly 2.8 V; when the tip moves from position A to the bottom of the pore (illustrated as position B), the direction of the induced friction force is upwards along the slope. Due to the deformation of the cantilever, however, a horizontal force and torsion moment are exerted on the tip to balance the contact load, friction force and applied normal load; the lateral force is thus reduced when the tip experiences a downhill motion. According to Fig. 6a, the Z signal shows an uphill motion between points B' and F', however, the lateral force increased and decreased considerably despite the Z gradient being fairly regular. The variation in lateral force can be explained by the fact that the tip was trying to follow the path of least resistance and some lateral movements were thus detected.

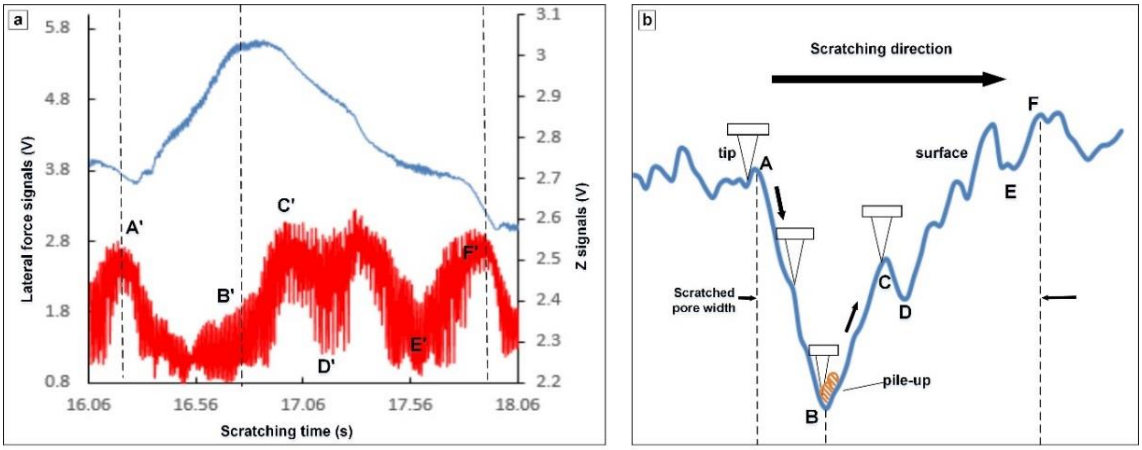

Fig. 6. Influence of pore surface on lateral-force distribution: (a) magnification of the detected lateral-force signals at a pore; (b) magnification of the contact relation between the tip and pore surface.

It should be noted that when the tip reached the bottom position B, the lateral voltage output was not the minimum value; instead, it was greater than the minimum value, which suggests that the minimum lateral force was reached before it reached the bottom position, while the tip scratched the keyhole pore. This is thought to be induced by the pile-up accumulation; that is, while the tip experiences a downhill motion, the generated pile-up may accumulate in front of the tip and settle at the bottom position. When the tip arrives at the bottom position, the accumulated pile-up can exert a force on the tip that increases the lateral force. It can be determined that the difference in the lateral voltage output between position A and the minimum (0.8 V) is roughly 2 V, and the friction-force difference induced by the downhill motion can be determined by Eq. (3); the difference is roughly up to 47.5 μN. When considering the applied normal force of 30 μN, we can conclude that the marked pore significantly influences the friction-force distribution during the AFM nanoscratching.

Since the keyhole pore plays an important role in lateral-force distribution, the friction-coefficient distribution would also be affected during AFM nanoscratching. The friction coefficient is the division of friction force by applied normal load; Fig. 7 shows the friction-coefficient distribution with respect to scratching time under different normal loads, varying from 10 μN to 40 μN. Fig. 7a shows the friction-coefficient distribution under a normal force of 10 μN; the friction coefficient fluctuated from 0.3 to 2.1, with an average value of 1.12. It should be noted, however, that apart from very limited positions with friction-coefficient values of less than 0.5,

the remainder of the scratched positions had a minimum friction coefficient of around 0.8. This can be explained by the pores that formed on the sample surface, which resulted in the jump of the friction coefficient; two typical pores are marked in the graph. The figure shows a magnified image of the friction-coefficient distribution that was affected by the pore; the figure also includes a trend line. A friction-coefficient fluctuation from 2 to 0.3 is thought to be induced by the marked keyhole pore; the irregularity of the pore surface is also implied by the trend line. Fig. 7b shows the friction-coefficient distribution under the normal load of 20 μN; the figure indicates a friction-coefficient distribution zone that was affected by a pore. Compared to Fig. 7a, a slight overall increase in the calculated friction coefficient was observed, and an average value of 1.26 was determined. With a continuous increase in applied normal load (from 30 μN to 40 μN), the average friction coefficient increased from 1.31 to 1.41, respectively (Figs. 7c and d).

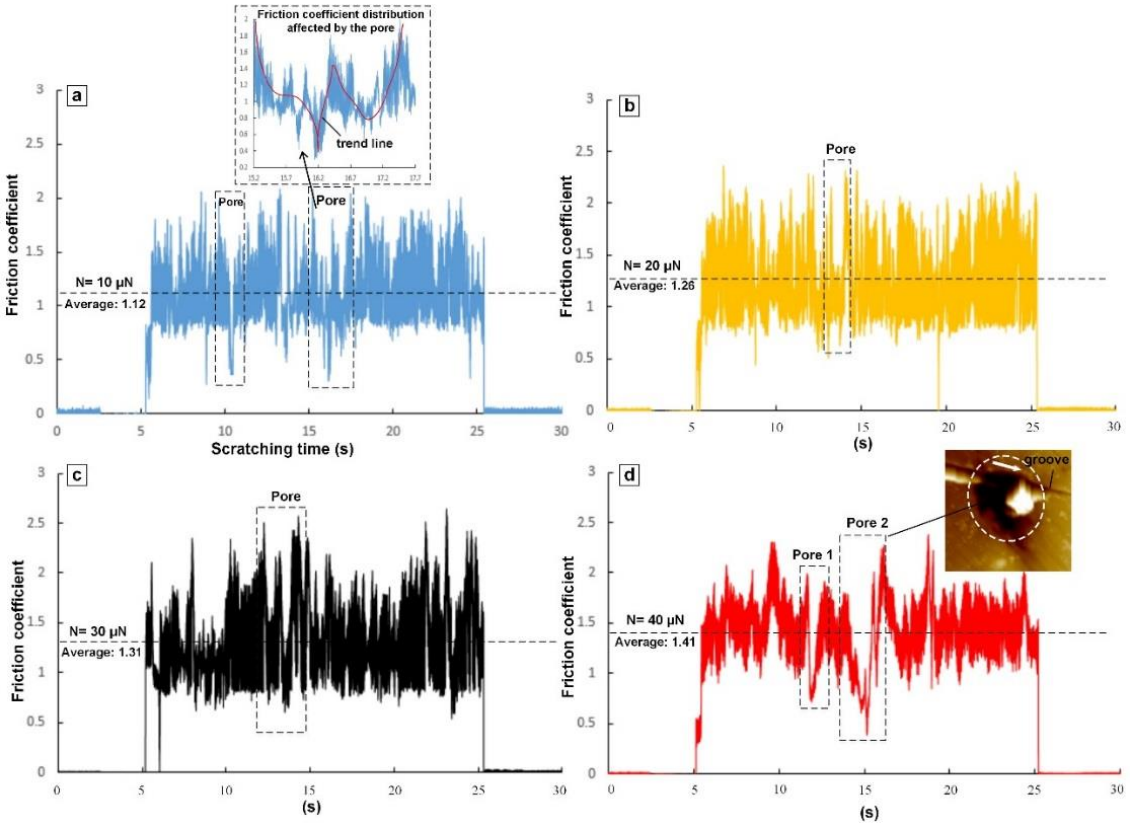

Fig. 7. Friction-coefficient distribution under normal loads of (a) 10 μN, (b) 20 μN, (c) 30 μN and (d) 40 μN.

In addition to the friction coefficient, another significant indicator that is often used to characterise nanoscale-friction behaviour during AFM nanoscratching is the

material wear rate. The wearing of the pyramidal diamond tip during the scratching was assumed to be zero in this work in order to calculate the material wear rate. Fig. 8 shows the measurements of the groove depth and width under an applied normal load of 30 μN. Fig. 8a shows a typical AFM image of a groove; three different positions (a, b and c) on the groove were chosen to determine the groove dimensions by averaging the three measurements. The cross-sectional profiles of the three marked positions are shown in Fig. 8b; the groove profile was assumed to be triangular when calculating the section area. As the figure shows, the three different positions shared nearly the same measured width (d') of 313 nm; the measured depth (h'), however, varied from 104 nm to 114 nm. This is thought to be due to the addition of nano-Al_2O_3 particulates, which offer higher hardness when the tip touches these particulates at the groove bottom; a relatively shallower depth could thus be obtained, such as the chosen position 'a' shown in Fig. 8a.

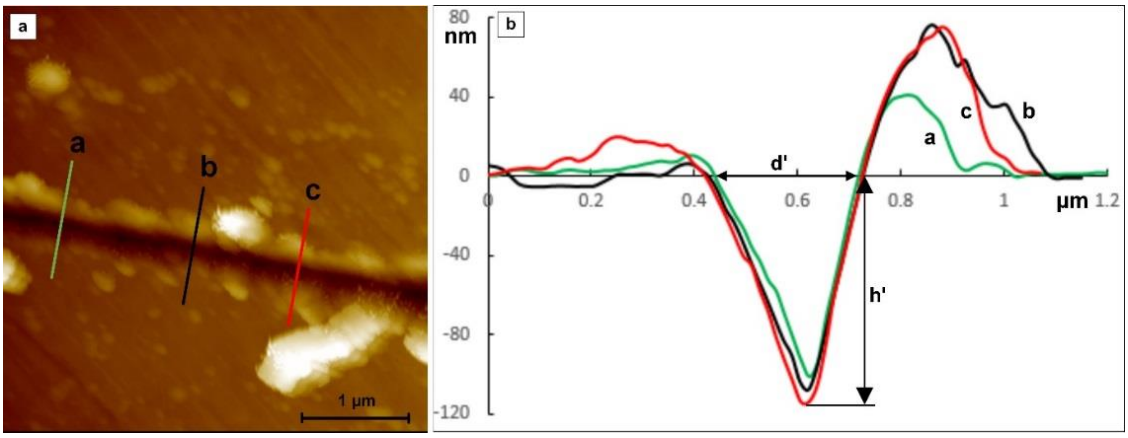

Fig. 8. Groove-dimension measurement: (a) typical AFM image of groove; (b) groove depth and width variation at three different positions under 30 μN. (For interpretation of the colour references, the reader is referred to the web version of this article.)

The averaged groove depth and width under normal loads from 10 μN to 40 μN are shown in Fig. 9a; the measured groove depth increased from 52 nm to 135.6 nm, while the groove width increased from 204 nm to 337 nm. Further, it can be determined that both groove depth and width offer a nearly linear correlation with applied normal load. The calculated material-wear rate and friction-coefficient variation in relation to applied normal load are shown in Fig. 9b. The figure shows that the wear rate increased from 5.3 $x10^{-4}$ to 5.7 x 10^{-4} mm^2/N as the normal load varied from 10 μN to 40 μN.

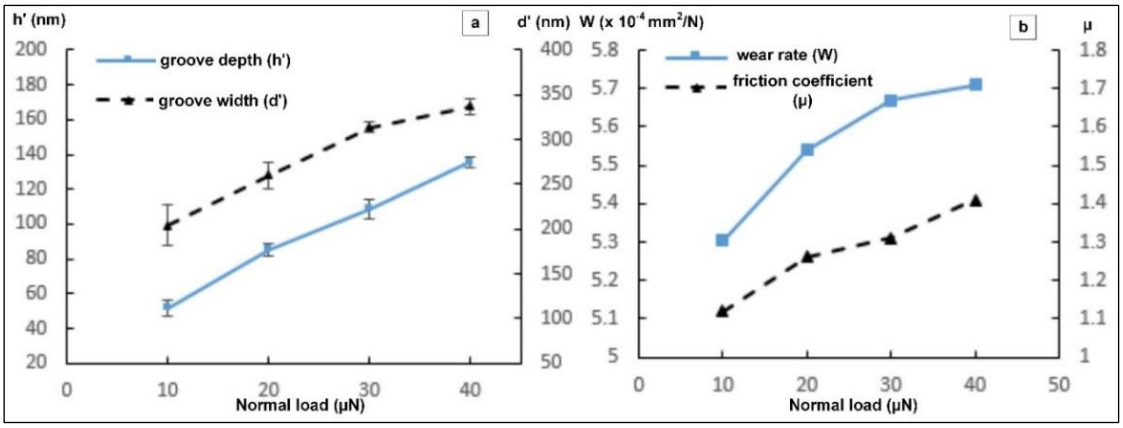

Fig. 9. Material wear-rate calculation with (a) measured groove dimensions and (b) calculated wear rate and friction coefficient in relation to normal load.

4. Discussion

4.1. Formation of keyhole pores

The as-fabricated cubic composite samples exhibited porosity and microcracks, as shown in Fig.1d. Keyholes are defects that occur during the SLM process. Parts should ideally be produced without them, since they tend to increase wear rates by reducing surface contact areas against opposing abrasive surfaces [29,30]. The formation of keyhole pores may be induced by the laser's working-mode transition from conduction to keyhole mode. This mechanism may be the dominating factor when relatively high laser power and low scanning speeds are employed when processing certain metal powders (e.g. aluminium and its alloys).

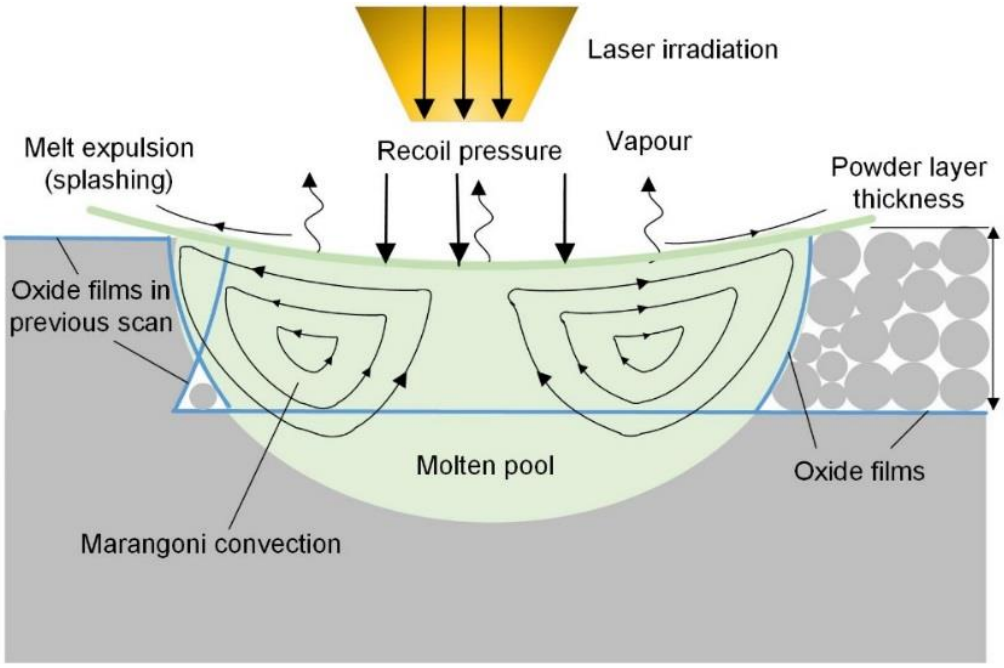

Fig. 10. Schematic diagram of laser-material interaction within the SLM process.

Fig. 10 shows the laser-material interaction within the molten pool. Due to the local difference of the surface tension induced by the temperature gradient, the liquid in the molten pool flowed from the high-temperature regions to the relatively cool region. Increasing the laser power and reducing the spot size have both been found to make the Marangoni convection stronger and move the centres of the cells closer to the pool edge [31]. When the temperature on the surface (T) becomes greater than the material's boiling point (T_b), strong vaporisation occurs; the induced recoil pressure, together with the Marangoni convection, causes a change in the molten pool shape and subsequent splashing. The collapse of the vapour cavity that is produced by the recoil pressure also results in the formation of keyhole pores; this process can be completed within 5 µs [32]. King et al. [33] have determined that, for a laser-spot size of tens of microns, the ejection of the molten material is independent of spot size. The condition $T = T_b$ can thus be considered to be the threshold for the generation of recoil pressure.

4.2. Wear rate and microhardness

The wear rates of the composite and pure Al specimens were determined to be 7 and 11.5 x 10^{-4} mm^3/Nm, respectively (Fig. 2d). Previous studies have found that the abrasive-wear resistance is proportional to the part's hardness; abrasive wear can thus be reduced by increasing the hardness of materials (e.g. via heat treatment) or

by reducing the normal load [19,34]. Fig. 11 shows the measured microhardness of the composite and pure Al samples as measured from 20 discrete locations. The averaged microhardness values of the composite and pure Al specimens were 48.35 and 40.75 HV/0.1, respectively. The 18.6% increase in the microhardness value of the composite sample is thought to have been induced by the addition of 4 vol.% Al_2O_3 reinforcement. This finding confirms the idea that the harder composite specimen would tend to exhibit better abrasive-wear behaviour than an unreinforced Al specimen.

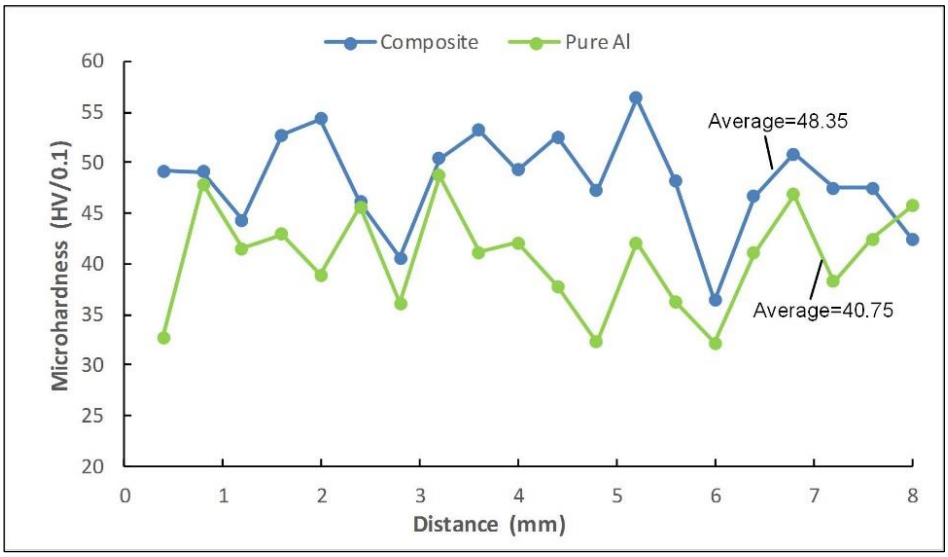

Fig. 11. Microhardness values of the composite and pure Al samples fabricated at 300 mm/s.

4.3. Nanoscale-wear behaviour with normal load

The AFM nanoscratching results indicated that the frictional coefficient increased with an increase in applied normal load (Fig. 7); this situation may be explained by a change of the contact condition and the adhesion force between the AFM tip and the specimen. Specifically, an increase in the normal load generally results in an increase in groove depth; when the groove depth is greater than the height of the diamond tip's spherical apex (with a tip radius of less than 40 nm), the dominant contact condition between the tip and the specimen becomes pyramidal rather than spherical. A pyramidal contact offers a larger contact area and further increases the adhesion force; an increase in adhesion force between tip and specimen thus leads to an increase in the friction force and friction coefficient. This finding is in agreement with [35], in which an AFM was used to investigate the fundamental micro-wear rate; that study found that the increase in adhesion force due to an increased contact area

caused the contact pressure to increase during the scratching when a Si_3N_4 tip was employed to scratch a Si specimen surface with an applied load from 10 to 800 nN.

According to the wear behaviour that the composite exhibited in this study (Fig. 9), the average groove depth (52 nm) under a 10 μN normal load was found to be slightly larger than the height of the diamond tip's spherical apex, with a tip radius of less than 40 nm (Fig. 9a). This situation implies that the contact condition included a spherical contact that was induced by the tip radius and pyramidal contact, which in turn was induced by the pyramidal shape of the tip. With an increase in the normal load to 40 μN, the groove depth increased and the pyramidal contact became the dominating contact condition. The increased contact area led to an increase in adhesion force and further contributed to an increase in the friction coefficient. This verifies the hypothesis that the increase in friction coefficient shown in Fig. 7 may be attributed to the change in the contact condition. The variation trend of the wear rate showed agreement with the friction coefficient trend; both can be explained by the change in contact condition within the AFM nanoscratching.

5. Conclusions

This study employed pin-on-disc tribometry and AFM nanoscratching to explore the macroscale and nanoscale wear behaviour of Al-Al_2O_3 nanocomposites that had been fabricated by selective laser melting. It investigated the influence of Al_2O_3 reinforcement on the macroscale wear behaviour of the as-fabricated specimens; it also examined pores that were formed within the SLM process on lateral-force and frictional-coefficient distribution during the nanoscratching process. The effects of applied normal load on the frictional coefficient and material-wear rate were also investigated. This paper has presented several important findings derived from the study's results, as follows.

(1) The added Al_2O_3 reinforcement contributed to the enhancement of macroscale wear behaviour. Compared to pure Al, a smaller wear rate for the composite specimen was achieved.
(2) Irregular pore surfaces may result in dramatic fluctuations in the frictional coefficient at the pore position during the AFM nanoscratching process. The measurements of single point contacts demonstrate that the presence of the

pores can significantly increase friction if asperities contacting the surface engage with them.

(3) The size effect and working-principle difference were both found to contribute to the difference in frictional coefficients at both the macroscale and the nanoscale. The recorded average frictional coefficient of the composite specimen under 1 N normal load was found to be 0.83 during the pin-on-disc sliding, while the average frictional coefficient during the AFM nanoscratching increased from 1.12 to 1.41 as the applied normal load varied from 10–40 μN.

(4) During the AFM nanoscratching, both average frictional coefficient and wear rate showed nearly linear correlation with applied normal load. This is thought to have been induced by the change of adhesion force and contact condition between the diamond tip and the tested specimen.

The experimental findings of this work will help to achieve an improved understanding of the macroscale and nanoscale friction and wear mechanisms that are affected by surface porosity and the reinforcements of the Al-Al_2O_3 composites that are often used in the aerospace and automotive industries. This study has also sought to expand the potential applications of the combination of additive manufacturing and atomic force microscopy in researching nanoscale wear behaviour. Part of the future work is exploring the macro and nanoscale wear behaviour of the composite samples with other ratios of Al and Al_2O_3 such as 92 vol.% Al and 8 vol.% Al_2O_3.

Acknowledgements

The authors would like to thank Dr Emmanuel Brousseau from Cardiff University for his assistance in the AFM experiments and Dr David Clark for the SEM operations. The lead author (Quanquan Han) gratefully appreciates the financial support of China Scholarship Council (CSC) and Cardiff University, UK.

References

[1] Ibrahim MF, Ammar HR, Samuel AM, Soliman MS, Samuel FH. On the impact toughness of Al-15 vol.% B4C metal matrix composites. Compos Part B Eng 2015;79:83–94. doi:10.1016/j.compositesb.2015.04.018.

[2] Miranda G, Buciumeanu M, Carvalho O, Soares D, Silva FS. Interface analysis and wear behavior of Ni particulate reinforced aluminum-silicon composites produced by PM. Compos Part B Eng 2015;69:101–10. doi:10.1016/j.compositesb.2014.09.017.

[3] Shin SE, Ko YJ, Bae DH. Mechanical and thermal properties of nanocarbon-reinforced aluminum matrix composites at elevated temperatures. Compos Part B Eng 2016;106:66–73. doi:10.1016/j.compositesb.2016.09.017.

[4] Prasad S V., Asthana R. Aluminum metal-matrix composites for automotive applications: Tribological considerations. Tribol Lett 2004;17:445–53. doi:10.1023/B:TRIL.0000044492.91991.f3.

[5] Karabulut Ş, Karakoç H, Çıtak R. Influence of B4C particle reinforcement on mechanical and machining properties of Al6061/B4C composites. Compos Part B Eng 2016;101:87–98. doi:10.1016/j.compositesb.2016.07.006.

[6] Kursun A, Bayraktar E, Enginsoy HM. Experimental and numerical study of alumina reinforced aluminum matrix composites: Processing, microstructural aspects and properties. Compos Part B Eng 2016;90:302–14. doi:10.1016/j.compositesb.2016.01.006.

[7] Kim HJ, Yoo SS, Kim DE. Nano-scale wear: A review. Int J Precis Eng Manuf 2012;13:1709–18. doi:10.1007/s12541-012-0224-y.

[8] Cho MH. The role of transfer film and back transfer behavior on the tribological performance of polyoxymethylene in sliding. J Mech Sci Technol 2009;23:2291–8.

[9] Geng Y, Yan Y, Yu B, Li J, Zhang Q, Hu Z, et al. Depth prediction model of nano-grooves fabricated by AFM-based multi-passes scratching method. Appl Surf Sci 2014;313:615–23. doi:10.1016/j.apsusc.2014.06.033.

[10] Chung KH, Kim DE. Wear characteristics of diamond-coated atomic force microscope probe. Ultramicroscopy 2007;108:1–10. doi:10.1016/j.ultramic.2007.01.016.

[11] Zhang F, Meng B, Geng Y, Zhang Y, Li Z. Friction behavior in nanoscratching of reaction bonded silicon carbide ceramic with Berkovich and sphere indenters. Tribol Int 2016;97:21–30. doi:10.1016/j.triboint.2016.01.013.

[12] Zou R, Xia Y, Liu S, Hu P, Hou W, Hu Q, et al. Isotropic and anisotropic elasticity and yielding of 3D printed material. Compos Part B Eng 2016;99:506–13. doi:10.1016/j.compositesb.2016.06.009.

[13] Farina I, Fabbrocino F, Carpentieri G, Modano M, Amendola A, Goodall R, et al. On the reinforcement of cement mortars through 3D printed polymeric and metallic fibers. Compos Part B Eng 2016;90:76–85. doi:10.1016/j.compositesb.2015.12.006.

[14] Gu D, Wang H, Dai D, Yuan P, Meiners W, Poprawe R. Rapid fabrication of Al-based bulk-form nanocomposites with novel reinforcement and enhanced performance by selective laser melting. Scr Mater 2015;96:25–8. doi:10.1016/j.scriptamat.2014.10.011.

[15] Gu DD, Meiners W, Wissenbach K, Poprawe R. Laser additive manufacturing of metallic components: materials, processes and mechanisms. Int Mater Rev 2012;57:133–64. doi:10.1179/1743280411Y.0000000014.

[16] Clare AT, Chalker PR, Davies S, Sutcliffe CJ, Tsopanos S. Selective laser melting of high aspect ratio 3D nickel-titanium structures two way trained for MEMS applications. Int J Mech Mater Des 2008;4:181–7. doi:10.1007/s10999-007-9032-4.

[17] Aboulkhair NT, Everitt NM, Ashcroft I, Tuck C. Reducing porosity in AlSi10Mg parts processed by selective laser melting. Addit Manuf 2014;1–4:77–86. doi:10.1016/j.addma.2014.08.001.

[18] Haboudou A, Peyre P, Vannes AB, Peix G. Reduction of porosity content generated during Nd: YAG laser welding of A356 and AA5083 aluminium alloys. Mater Sci Eng A 2003;363:40–52. doi:10.1016/S0921-5093(03)00637-3.

[19] Kang N, Coddet P, Liao H, Baur T, Coddet C. Wear behavior and microstructure of hypereutectic Al-Si alloys prepared by selective laser melting. Appl Surf Sci 2016;378:142–9. doi:10.1016/j.apsusc.2016.03.221.

[20] Jue J, Gu D, Chang K, Dai D. Microstructure evolution and mechanical properties of Al-Al2O3 composites fabricated by selective laser melting. Powder Technol 2017;310:80–91. doi:10.1016/j.powtec.2016.12.079.

[21] Sun Y, Moroz A, Alrbaey K. Sliding wear characteristics and corrosion behaviour of selective laser melted 316L stainless steel. J Mater Eng Perform 2014;23:518–26. doi:10.1007/s11665-013-0784-8.

[22] Baradeswaran a., Elaya Perumal a. Study on mechanical and wear properties of Al 7075/Al2O3/graphite hybrid composites. Compos Part B Eng 2014;56:464–71. doi:10.1016/j.compositesb.2013.08.013.

[23] Iacob G, Ghica VG, Buzatu M, Buzatu T, Petrescu MI. Studies on wear rate and micro-hardness of the Al/Al2O3/Gr hybrid composites produced via powder metallurgy. Compos Part B Eng 2014. doi:10.1016/j.compositesb.2014.07.008.

[24] Han Q, Setchi R, Evans SL. Synthesis and characterisation of advanced ball-milled Al-Al2O3 nanocomposites for selective laser melting. Powder Technol 2016;297:183–92. doi:10.1016/j.powtec.2016.04.015.

[25] Han Q, Setchi R, Evans SL. Characterisation and milling time optimisation of nanocrystalline aluminium powder for selective laser melting. Int J Adv Manuf Technol 2017;88:1429–38. doi:10.1007/s00170-016-8866-z.

[26] Wang F, Zhao X. Effect of contact stiffness on wedge calibration of lateral force in atomic force microscopy. Rev Sci Instrum 2007;78:43701. doi:10.1063/1.2720723.

[27] Varenberg M, Etsion I, Halperin G. An improved wedge calibration method for lateral force in atomic force microscopy. Rev Sci Instrum 2003;74:3362–7. doi:10.1063/1.1584082.

[28] Kimura T, Nakamoto T, Mizuno M, Araki H. Effect of silicon content on densification, mechanical and thermal properties of Al-xSi binary alloys fabricated using selective laser melting. Mater Sci Eng A 2017;682:593–602. doi:10.1016/j.msea.2016.11.059.

[29] Kang N, Coddet P, Chen C, Wang Y, Liao H, Coddet C. Microstructure and wear behavior of in-situ hypereutectic Al-high Si alloys produced by selective laser melting. Mater Des 2016;99:120–6. doi:10.1016/j.matdes.2016.03.053.

[30] Deshpande PK, Lin RY. Wear resistance of WC particle reinforced copper matrix composites and the effect of porosity. Mater Sci Eng A 2006;418:137–45. doi:10.1016/j.msea.2005.11.036.

[31] Limmaneevichitr C, Kou S. Visualization of Marangoni convection in simulated weld pools containing a surface-active agent. Weld J 2000;79:324s–330s.

[32] Khairallah SA, Anderson AT, Rubenchik A, King WE. Laser powder-bed fusion additive manufacturing: Physics of complex melt flow and formation mechanisms of pores, spatter, and denudation zones. Acta Mater 2016;108:36–45.

[33] King WE, Barth HD, Castillo VM, Gallegos GF, Gibbs JW, Hahn DE, et al. Observation of keyhole-mode laser melting in laser powder-bed fusion additive manufacturing. J Mater Process Technol 2014;214:2915–25. doi:10.1016/j.jmatprotec.2014.06.005.

[34] Sharma S, Bijwe J, Panier S. Assessment of potential of nano and micro-sized boron carbide particles to enhance the abrasive wear resistance of UHMWPE. Compos Part B Eng 2016;99:312–20. doi:10.1016/j.compositesb.2016.06.003.

[35] Chung KH, Kim DE. Fundamental investigation of micro wear rate using an atomic force microscope. Tribol Lett 2003;15:135–44. doi:10.1023/A:1024457132574.